Gyrokinetic particle-in-cell simulations of electromagnetic turbulence in the presence of fast particles and global modes

A. Mishchenko[(1)], **A. Bottino**[(2)], **T. Hayward-Schneider**[(2)],
E. Poli[(2)], **X. Wang**[(2)], **R. Kleiber**[(1)], **M. Borchardt**[(1)],
C. Nührenberg[(1)], **A. Biancalani**[(3)], **A. Könies**[(1)], **E. Lanti**[(4)],
Ph. Lauber[(2)], **R. Hatzky**[(2)], **F. Vannini**[(2)], **L. Villard**[(5)], **and**
F. Widmer[(6,2)]

[(1)]Max Planck Institute for Plasma Physics, D-17491 Greifswald, Germany
[(2)]Max Planck Institute for Plasma Physics, D-85748 Garching, Germany
[(3)]Léonard de Vinci Pôle Universitaire, Research Center, 92 916 Paris La Défense, France
[(4)]Ecole Polytechnique Fédérale de Lausanne, SCITAS, CH-1015 Lausanne, Switzerland
[(5)]Ecole Polytechnique Fédérale de Lausanne, Swiss Plasma Center (SPC), CH-1015 Lausanne, Switzerland
[(6)]International Research Collaboration Center, National Institutes of Natural Sciences, 105-0001 Tokyo, Japan

E-mail: `alexey.mishchenko@ipp.mpg.de`

Abstract. Global simulations of electromagnetic turbulence in circular-flux-surface tokamak and ASDEX-Upgrade geometry, tearing instabilities and their combination with the electromagnetic turbulence, nonlinear Alfvénic modes in the presence of fast particles and their combination with the electromagnetic turbulence, and global electromagnetic turbulence in Wendelstein 7-X stellarator geometry are carried out using the gyrokinetic particle-in-cell codes ORB5 (E. Lanti et al, Comp. Phys. Comm., **251**, 107072 (2020)) and EUTERPE (V. Kornilov et al, Phys. Plasmas, **11**, 3196 (2004)). Computational feasibility of simulating such complex coupled systems is demonstrated. For simplicity, reduced mass ratio is used throughout the paper.

1. Introduction

Creation and control of burning plasmas is an ultimate goal of the magnetic fusion worldwide effort. Such plasmas will become experimentally accessible in the foreseeable future when the ITER and SPARC facilities start their operation. One of the characteristic features of the burning plasmas is the intrinsic richness of their physics featuring

complex couplings and interactions of the microscopic processes (turbulence) with the macroscopic ones (MHD and Alfvénic modes). These interactions can affect properties of the turbulence as well as the evolution of macroscopic instabilities. Such couplings may become especially strong in burning plasmas where fast particles are abundant since they can drive the macroscopic modes unstable. A global approach is needed to assess the physics combining macroscopic modes and turbulence. Under the "global approach" we understand the full-torus simulations throughout this paper.

Global simulations of the electromagnetic turbulence can be particularly difficult due to the variety of the physics involved, but also as a consequence of the numerical problems, such as the cancellation problem [1, 2]. Involving all the relevant time scales ranging from the electron motion to slow MHD dynamics (e.g. growth and nonlinear evolution of the tearing instability) and electromagnetic turbulence adds to the computational difficulty of the global gyrokinetic simulations in the electromagnetic regime. Addressing this problem in its full complexity for the reactor-scale plasma will require the emerging exascale computing. However, first steps in this direction can already be made now using the existing high-performing computing systems and employing the available codes. This has been the main goal of the PRACE computing project EMGKPIC. In this paper we report on the basic approach and the main results of the project. Because of the limited space, the results will be described in a brief manner leaving details to follow-up publications.

In the project, the global gyrokinetic particle-in-cell codes ORB5 [3] and EUTERPE [4] have been used to simulate electromagnetic turbulence in realistic tokamak and stellarator geometries. Demonstrating feasibility of global turbulence simulations using the electromagnetic gyrokinetic PIC codes was the first goal of the project. The global setup permits combining electromagnetic turbulence with global modes, such as tearing instabilities and Alfvénic Eigenmodes in the presence of the energetic particles. Assessing such combinations and affordability of their simulations was another goal of the project. A particularly strong emphasis has been put on the simulations of electromagnetic turbulence which is known to be notoriously challenging in a global setup. Combining it with the macroscopic physics (Alfvénic and MHD) is less difficult if the turbulence problem is solved. The following "case studies" have been identified:

(i) global electromagnetic turbulence in circular-flux-surface tokamak and ASDEX-Upgrade tokamak geometry

(ii) tearing instabilities and their combination with the electromagnetic turbulence

(iii) nonlinear Alfvénic modes in the presence of fast particles and their combination with the electromagnetic turbulence

(iv) global electromagnetic turbulence in Wendelstein 7-X stellarator geometry

The ORB5 and EUTERPE codes share the equations solved, the basic discretization principles, and many aspects of technical implementation (see Ref. [5] for details). Despite these similarities, they remain separate projects with a different set of capabilities. Out of these two codes, only EUTERPE can address stellarator geometries.

On the other hand, tokamak simulations using ORB5 are normally more efficient due to the tokamak axisymmetry explicitly employed in the code. Therefore in the project, all tokamak simulations have been performed using ORB5 and all stellarator simulations using EUTERPE.

In this paper, we report global electromagnetic simulations solving gyrokinetic equations and employing the numerical schemes described in detail in Ref. [5]. According to the "case studies" selected and described above, the first basic component considered in these simulations is electromagnetic turbulence nonlinearly evolving and saturating through zonal flow excitation or relaxation of the plasma profiles. In the finite-beta regime, the Kinetic Ballooning Mode (KBM) turbulence is believed to play an important role [6, 7, 8, 9, 10, 11, 12, 13]. We identify the KBM regime performing parameter scans with respect to the plasma beta. We compare the low-beta Ion-Temperature-Gradient driven (ITG) turbulence with the KBM turbulence at a higher beta in the same magnetic configuration and for the same plasma profile shape. The second basic component of the global physics considered here is an MHD perturbation, namely the collisionless tearing mode, coupled to electromagnetic turbulence. We provide an example of this instability evolving separately and in the presence of the background turbulence. A basic feasibility of such simulations is demonstrated. The third component of the global physics is associated with macroscopic nonlinear Alfvénic Eigenmodes destabilized by the fast particles. Frequency evolution of a Toroidal Alfvén Eigenmode in the presence of electromagnetic turbulence is considered. Finally, the electromagnetic turbulence in non-axisymmetric stellarator geometry is addressed and feasibility of stellarator simulations is demonstrated. These examples encompass the physics content computationally available for future in-depth studies using ORB5 and EUTERPE. In this paper, we omit collisions. The simulations are carried out until the heat fluxes saturate and the profile relaxation stops. For simplicity, we use the reduced mass ratio $m_i/m_e = 200$ throughout this paper. Extending the simulations to the realistic mass ratio does not normally pose a problem, see Ref. [5]. Of course, such simulations take longer because of a smaller time step needed. The high computational cost of the simulations shown here has made it difficult to perform extensive in-depth convergence studies. Typically, we have run our simulations at the limit set by the hardware (for example, the size of the GPU memory or the overall duration of a simulation).

The structure of this paper is as follows. In Sec. 2, we consider electromagnetic turbulence in tokamak plasmas. In Sec. 3, the evolution of the tearing mode in the presence of electromagnetic turbulence is addressed. In Sec. 4, the coupled nonlinear system including Alfvén Eigenmodes, fast particles, and turbulence is considered. In Sec. 5, the stellarator simulations are described. Finally, conclusions are made in Sec. 6.

2. Electromagnetic turbulence in tokamak plasmas

In this Section, we consider global electromagnetic turbulence, in particular the

transition from the ITG to the KBM regime. The KBM instabilities and turbulence received a lot of attention because of their potential importance in high-beta plasmas, such as envisioned for a fusion reactor. It has been suggested [7, 14, 15] that zonal flow generation by the KBM turbulence can be suppressed at larger beta due to the field line stochasticity induced by the magnetic component of the electromagnetic turbulence leading to the "electromagnetic run-away" observed in the flux-tube simulations [14]. In addition, there is a counteraction of the Reynolds stress by the Maxwell stress in nonlinear evolution of the electromagnetic instabilities [12] weakening the zonal flows as well. On the other hand, the global gyrokinetic KBM simulations [11, 12] report that the zonal flows are still of crucial importance also for saturation of the KBM turbulence.

First, we consider tokamak geometry with the aspect ratio $A = 10$, cirular cross-sections, the safety factors $q(\rho) = 0.8 + 0.8\rho^2$ and $q(\rho) = 1.1 + 0.8\rho^2$ (two cases compared), where ρ is the radius of the circular flux surface. We employ an "ad-hoc" tokamak equilibrium defined using the relations: $\boldsymbol{B} = \nabla\psi \times \nabla\varphi + I\nabla\varphi$ with $I = B_0 R_0$, $\psi(\rho) = \int_0^\rho B_0 \rho' \mathrm{d}\rho'/q(\rho')$, and φ the toroidal angle. Here, $B_0 = 1$ T is the magnetic field at the axis, $R_0 = 1$ m is the major radius, and $q(\rho)$ is the safety factor profile. Note that it is a well-known practical difficulty to reconcile the profiles suitable for gyrokinetics (normally with the gradients vanishing at the axis and towards the plasma edge) and the profiles suitable for the equilibrium codes (normally polynomial ones with the gradient more homogeneously distributed in the radial direction). In our simulations, the temperature and density profiles are defined by the expressions:

$$n_{0s}(s)/n_{0s}(s_0) = \exp\left[-\kappa_\mathrm{n}\Delta_\mathrm{n}\tanh\left(\frac{s - s_0}{\Delta_\mathrm{n}}\right)\right] \tag{1}$$

$$T_{0s}(s)/T_{0s}(s_0) = \exp\left[-\kappa_\mathrm{T}\Delta_\mathrm{T}\tanh\left(\frac{s - s_0}{\Delta_\mathrm{T}}\right)\right] \tag{2}$$

Here, $s = \sqrt{\psi/\psi_a}$, ψ is the poloidal magnetic flux, ψ_a is the poloidal magnetic flux at the plasma edge, $s_0 = 0.5$, $\kappa_\mathrm{n} = 0.3$, and $\Delta_\mathrm{T} = \Delta_\mathrm{n} = 0.208$. Two different temperature gradients will be considered corresponding to $\kappa_\mathrm{T} = 1.0$ and $\kappa_\mathrm{T} = 2.0$. The ubiquitous nonlinear generation of the small scales in the phase space (filamentation) is controlled with the Krook operator, see Ref. [16] for further details. The machine size is determined by $L_x = 2r_\mathrm{a}/\rho_\mathrm{s} = 360$ with r_a the minor radius and ρ_s the characteristic bulk-ion sound gyroradius, the ion-to-electron mass ratio is $m_\mathrm{i}/m_\mathrm{e} = 200$. The character of the turbulence is defined by the plasma β: the electromagnetic-ITG regime for small β changing into the KBM regime when β increases. Here, the plasma $\beta = 2\mu_0 n_0(T_{i0} + T_{e0})/B_0^2$ is defined using the profiles computed at the mid-radius of the tokamak and the magnetic field computed at the magnetic axis. The ad-hoc tokamak equilibrium remains fixed for all plasma β. The transition from the ITG to the KBM regime is shown in Fig. 1 where the linear growth rate is plotted as a function of β. This transition has been known since some time already and documented in several papers [6, 7, 8, 9]. The critical threshold beta value for KBM depends on several parameters such as the magnetic shear, and is typically slightly below the ideal MHD ballooning

limit [6, 10, 13]. The growth rate is computed from the linear evolution of the perturbed energy flux. The radial fluxes are calculated throughout the paper as averages in the radial domain $0.3 \leq s \leq 0.7$. The simulations are performed in the full torus $0 \leq s \leq 1$ including the magnetic axis. One sees a characteristic ITG-KBM transition for different plasma temperature and safety factor profiles.

Considering now the nonlinear evolution, it has been known for some time that simulations in the KBM regime are particularly challenging [7, 14, 9]: sometimes a numerical instability appears in the long-time limit, making simulations impractical at beta values too high above the KBM threshold. In the following, we shall demonstrate that with our current numerical approach, nonlinear global EM simulations can achieve stable saturated conditions with beta values much larger than the KBM threshold. The nonlinear evolution of the radial perturbed energy flux is shown in Fig. 2 for the both regimes. The total number of the ion markers is $N_i = 400\,000\,000$ and the total number of the electron markers is $N_e = 1\,000\,000\,000$. We have used 256 grid points in the radial direction, 320 grid points in the poloidal direction, and 192 grid points in the toroidal direction. The Fourier filter has been applied with the mode numbers $-40 \leq n \leq 40$ kept in the toroidal filter. For the poloidal modes, the diagonal filter has been used with the width of 11 modes centered at the resonant poloidal mode number satisfying the condition $m_{res} = q(s)n$ for a given toroidal mode number n at a given flux surface s. The time step $\Delta t = 2\omega_{ci}^{-1}$ has been used. The Krook operator with the decay rate $\gamma_K = 10^{-4}\omega_{ci}$ is applied for the both species. The simulation duration is typically several days (several times 24 hours) on 32 nodes of Marconi100 (4 MPI tasks per node, 32 CPU cores per MPI task, 4 NVIDIA Volta V100 GPUs per node). For the realistic mass ratio, the simulation would take more than a week since the time step, proportional to $\sqrt{m_e/m_i}$, would have to be reduced accordingly. Naturally, longer simulation times would cause an increased overhead related to the job scheduler queues and increase a risk of the hardware failure.

In Fig. 2, one sees that the simulation enters the nonlinear phase after the linear growth in both (a) the ITG regime and (b) the KBM regime. The latter case shows a decaying oscillatory relaxation dynamics possibly resulting from the avalanche-like temperature profile evolution (profile flattening which starts at the position of the maximum temperature gradient and propagates radially). An animation showing this profile evolution is available online. In Fig. 2(b), the oscillations in the energy flux decay probably due to the temperature profile evolving to the marginal one. This profile evolution is itself an interesting topic for future research. In the present paper, we establish a "technical route" to such simulations. As can be seen, our nonlinear simulations show no sign of numerical instability, even in the KBM regime. Note that the end time of the KBM case, Fig. 2(b), is $(c_s/a)t \approx 120$.

This profile relaxation process is also indicated by the evolution of the electrostatic potential shown in Fig. 4. One sees here how the finger-like structures (reminiscent to the "detonation" events [17, 18]) develop and propagate outwards resulting in a flattening of the temperature profile shown in Fig. 5(b). At later times, the temperature

profile steepens at another radial location leading to the next relaxation cycle. In contrast, the ITG regime shows a much weaker relaxation of the temperature profile, see Fig. 5(a). The electrostatic potential of the ITG turbulence, shown in Fig. 3, develops the characteristic pattern of the turbulent eddies decorrelated by the zonal flow. Note that the global linear mode (its envelope) usually has an extent comparable to the temperature profile "length" (the region of finite gradient). This can be seen in Fig. 3 at $\omega_{ci}t = 10\,000$, for example, for the temperature profile shown in Fig. 5(a). This length is normally a fraction (e.g. 1/3) of the plasma diameter. In sound gyro-radii, this implies that the size of the "active" region is roughly $120\rho_s$ for the case shown in Fig. 3 at $\omega_{ci}t = 10\,000$. This original "linear eddy" size can be broken into smaller "nonlinear eddies" by the zonal flow as can be seen in Fig. 3 at $\omega_{ci}t = 16\,000$ showing the nonlinear stage of the electromagnetic ITG. The zonal flow appears to be much less pronounced in the KBM case, shown in Fig. 4, where the "eddy" (the finger-like structure) is "expelled" out of the active destabilization region instead of being "broken". This evolution is accompanied by a strong temperature profile relaxation, shown in Fig. 5(b). The evolution of the density profile is shown in Fig. 6.

We point out that the role of zonal flows (and zonal fields) in the KBM saturation has been the object of some controversy, flux-tube simulations coming to apparently contradictory conclusions [6, 8]. For simulations and analysis of KBM saturation in a global gyrokinetic approach, see Ref. [11, 12, 19, 5]. Note that the profile relaxation seems to be important for the turbulence saturation in the case considered here, similar to Ref. [20]. In this paper, we use the KBM label for the nonlinear simulations based on the linear onset of the instability. In future, an in-depth analysis will be carried out to support our assessment that the higher beta case is truly in a nonlinear KBM regime. Here, we have already observed a very different profile evolution and substantial differences in the structure of the electrostatic potential in the nonlinear stage of the high-beta case compared to the low-beta one clearly showing a transition in the turbulence regime.

As a next step, consider a realistic ASDEX-Upgrade equilibrium corresponding to the "NLED-AUG" case [21], down-scaled to $L_x = 300$, with the safety factor profile shown in Fig. 7(a); temperature and density profiles shown in Figs. 11 and 12. The total number of the ion markers is $N_i = 500\,000\,000$ and the total number of the electron markers is $N_e = 500\,000\,000$. We have used 288 grid points in the radial direction, 704 grid points in the poloidal direction, and 192 grid points in the toroidal direction. The Fourier filter has been applied with the mode numbers $-40 \le n \le 40$ kept in the toroidal filter. For the poloidal modes, the diagonal filter has been used with the width of 15 modes centered at the resonant poloidal mode number satisfying the condition $m_{res} = q(s)n$ for a given toroidal mode number n at a given flux surface s. The time step $\Delta t = \omega_{ci}^{-1}$ has been used. The Krook operator with the decay rate $\gamma_K = 10^{-4}\omega_{ci}$ is applied for the both species. The simulation duration is typically a week (seven days 24 hours each) on 128 nodes of Marconi (48 Intel SKL cores per node). Similarly to the previous case, a single simulation would take considerably longer than a week for
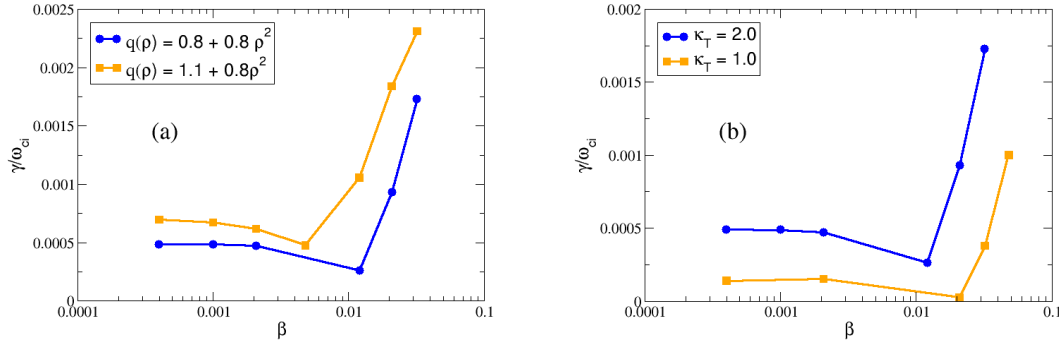
Figure 1. Growth rate computed from the linear phase of the perturbed energy flux evolution (including effect of multiple Fourier modes) plotted as a function of β. One clearly sees the characteristic ITG-KBM transition. (a) Temperature and density gradients $\kappa_T = 2.0$, $\kappa_n = 0.3$, safety factor profile $q(\rho) = 0.8 + 0.8\rho^2$ compared to $q(\rho) = 1.1 + 0.8\rho^2$. (b) Density gradient $\kappa_n = 0.3$, safety factor $q(\rho) = 0.8 + 0.8\rho^2$, temperature gradient $\kappa_T = 2.0$ compared to $\kappa_T = 1.0$.
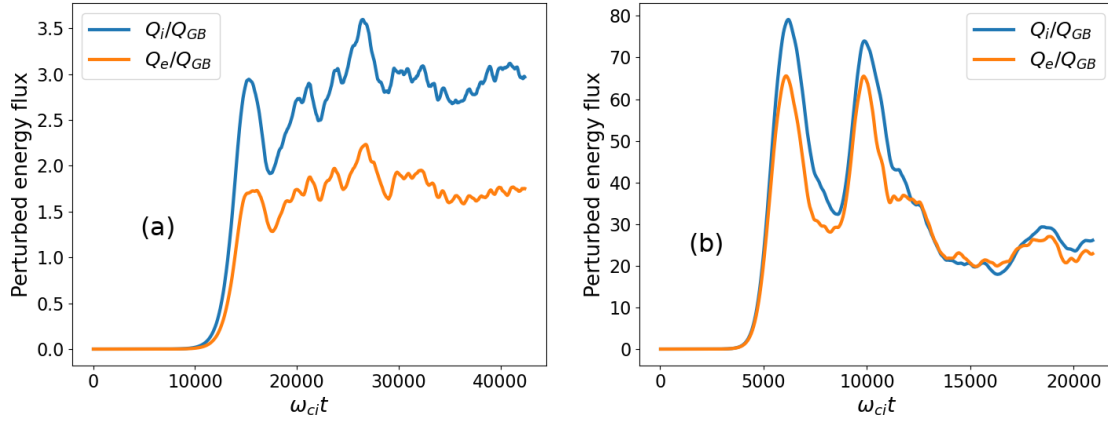
Figure 2. Perturbed energy flux evolution for the safety factor $q(\rho) = 1.1 + 0.8\rho^2$, the temperature gradient $\kappa_T = 2.0$, (a) $\beta = 0.1\%$ (electromagnetic ITG regime), and (b) $\beta = 2.08\%$ (KBM regime). The energy flux is considerably larger in the KBM regime.
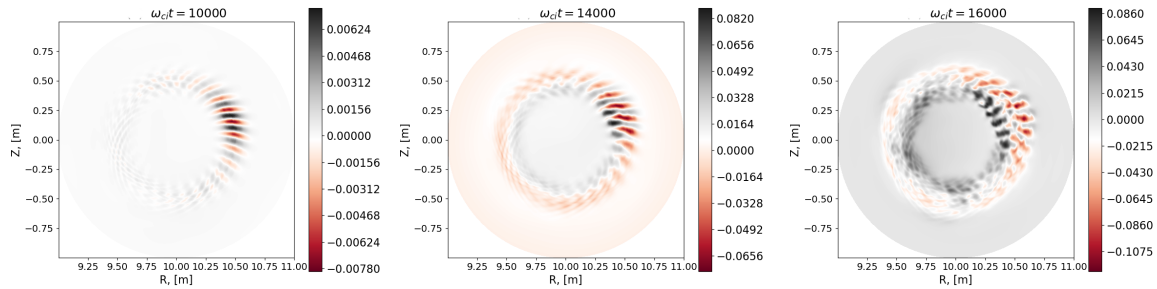
Figure 3. Evolution of the electrostatic potential in the ITG turbulence shown in Fig. 2(a). One sees how the zonal flow develops and decorrelates the turbulent eddies. Zonal flow dynamics determines the saturation of the electromagnetic ITG turbulence.
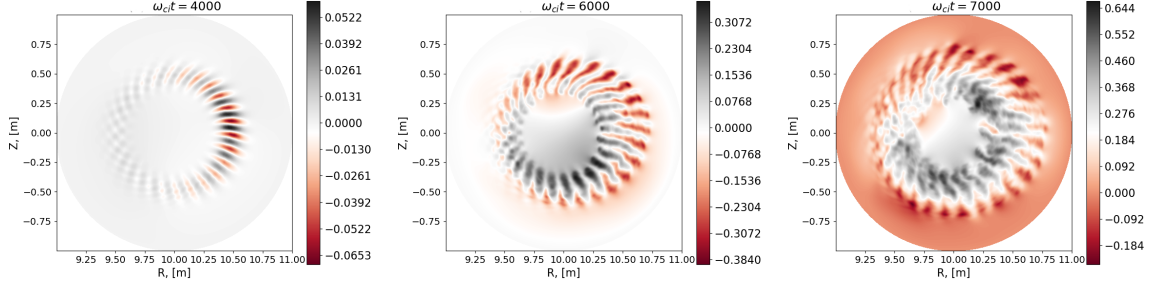
Figure 4. Evolution of the electrostatic potential in the KBM turbulence shown in Fig. 2(b). One sees the finger-like structures developing and propagating outwards. Plasma profile relaxation, Fig. 5, determines the saturation of the KBM turbulence.
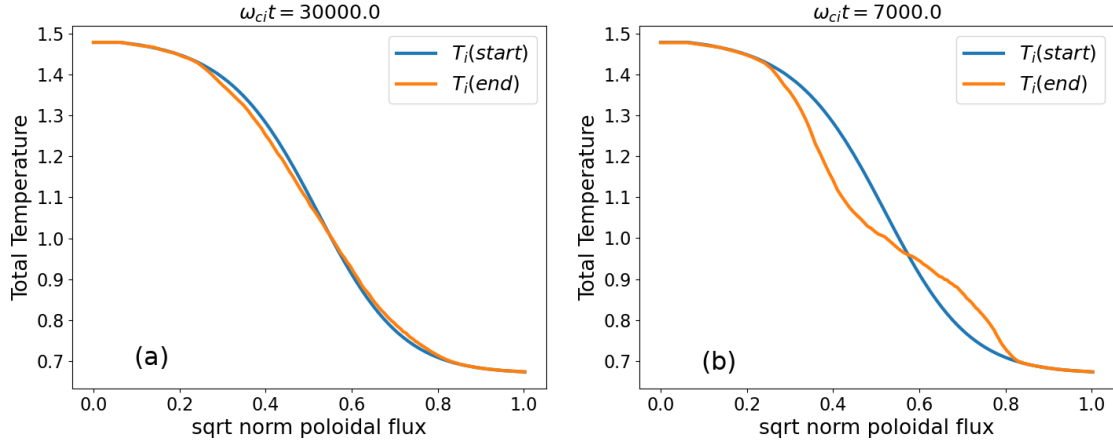

Figure 5. Temperature relaxation in (a) the ITG regime ($\beta = 0.1\%$, $k_T = 2.0$, $q(\rho) = 1.1 + 0.8\rho^2$), and (b) the KBM regime ($\beta = 2.08\%$, $k_T = 2.0$, $q(\rho) = 1.1 + 0.8\rho^2$). The profile relaxation is much weaker for the ITG turbulence than in the KBM case.
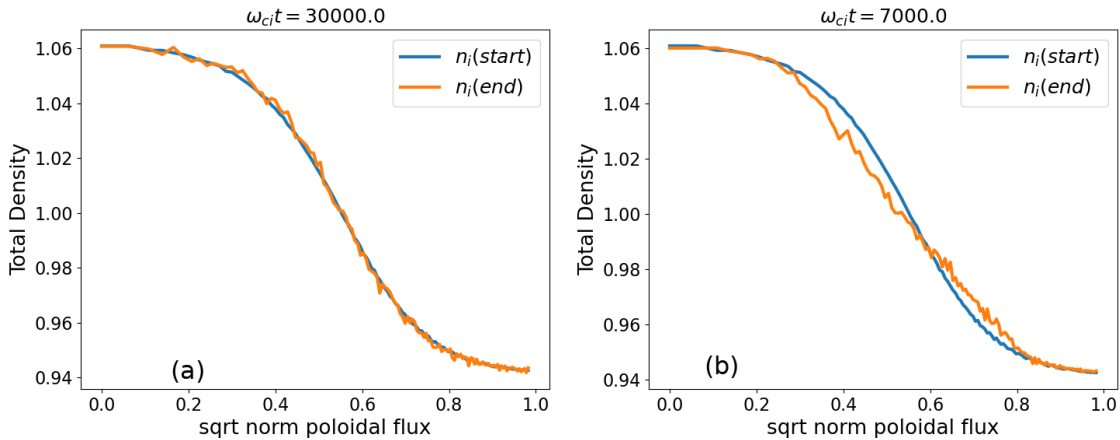
Figure 6. The density profile relaxation for (a) the ITG turbulence and (b) the KBM turbulence. The simulation parameters are as in Fig. 5.

the realistic mass ratio. As in the previous case, the ITG-KBM transition can be seen in Fig. 7(b) where the growth rate is shown as a function of plasma β. The growth rate is computed using the linear phase of the perturbed energy flux evolution. The magnetic equilibrium is fixed to the "NLED-AUG" case [21] for all values of plasma β. The perturbed energy flux is shown in Fig. 8(a) for the ITG regime and in Fig. 8(b) for the KBM regime. One can see that the energy flux has entered the nonlinear phase of its evolution. The values of the flux measured in the gyro-Bohm units are comparable in both regimes. The nonlinear energy flux oscillations appearing in Fig. 8 may result from the profile evolution. Particularly, from the nonlinear radial movement of the position of the maximum temperature gradient. In addition, there can be an interplay between the profile evolution, linear stability, and the zonal flow generation complicating the picture. We will address this subject in detail elsewhere.

The evolution of the electrostatic potential is shown in Fig. 9 for the ITG regime, and in Fig. 10 for the KBM regime. No distinct finger-like structures are observed in this case indicating a possible relevance of zonal flows, for the parameters considered, also in the KBM regime as Refs. [12, 11] suggest. Note that the zonal flow suppression [14] in the electromagnetic regime should depend on the strength of the magnetic component in the field perturbation and also on the effectiveness of the parity mixing [9, 22] which can be parameter-dependent (e. g. depending on the plasma aspect ratio and shaping). We will address this subject in future.

The temperature and density nonlinear profile evolution is plotted in Figs. 11 and 12. One can see that the temperature profile relaxation caused by the KBM turbulence is not very strong for the shaped ASDEX-Upgrade geometry, in contrast to the circular cross-section tokamak case shown in Fig. 5(b). This weaker profile relaxation may be related to a higher MHD stability of the shaped tokamak plasmas. We will consider this subject in detail elsewhere. In Fig. 12(a), one can see a density peaking corresponding to a turbulent particle pinch in the ITG regime which is in a qualitative agreement with Ref. [23]. In contrast for the KBM turbulence, the particle flux is outward, see the density profile in Fig. 12(b). Note that there is a weak particle pinch also for the large-aspect ratio tokamak case in the ITG regime. It can be barely seen in Fig. 6(a). Note that decrease of the turbulence-induced density peaking with the aspect ratio is in agreement with the curvature pinch mechanism [24]. The particle flux reverses its sign in the KBM regime in the both tokamak geometries considered here. In future work, the question of the particle fluxes driven by the electromagnetic turbulence will be addressed in more detail. In this paper, we limit our consideration to the relatively early nonlinear phase. The main task is to demonstrate that the turbulence enters this nonlinear stage without severe complications even in the high-beta KBM regime up to values (4.8%) three times higher than the linear KBM threshold. No indications of such complications have been observed in the simulations described here. The late nonlinear stage which would result from a very long nonlinear run is out of the scope of this paper primarily because of a high computational cost and a very high resolution which would be required in such simulations. We leave this task to the future work.
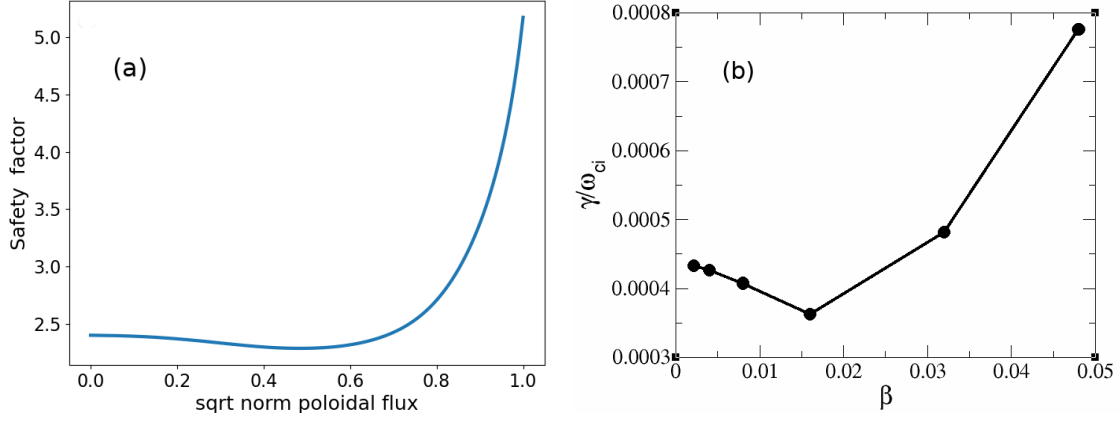
Figure 7. (a) The safety factor of the "NLED-AUG" case [21]. (b) The growth rate in the ASDEX-Upgrade plotted as a function of plasma β. One can see the ITG-KBM transition similar to the circular case. The growth rate is computed using the linear phase of the perturbed energy flux evolution.
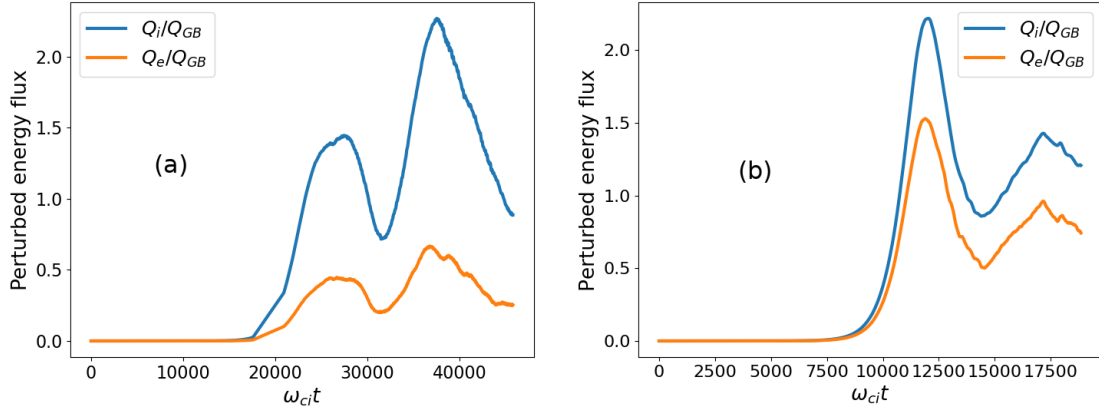

Figure 8. The perturbed energy flux in the ASDEX-Upgrade for (a) the ITG regime, $\beta = 0.4\%$, and (b) the KBM regime, $\beta = 4.8\%$.
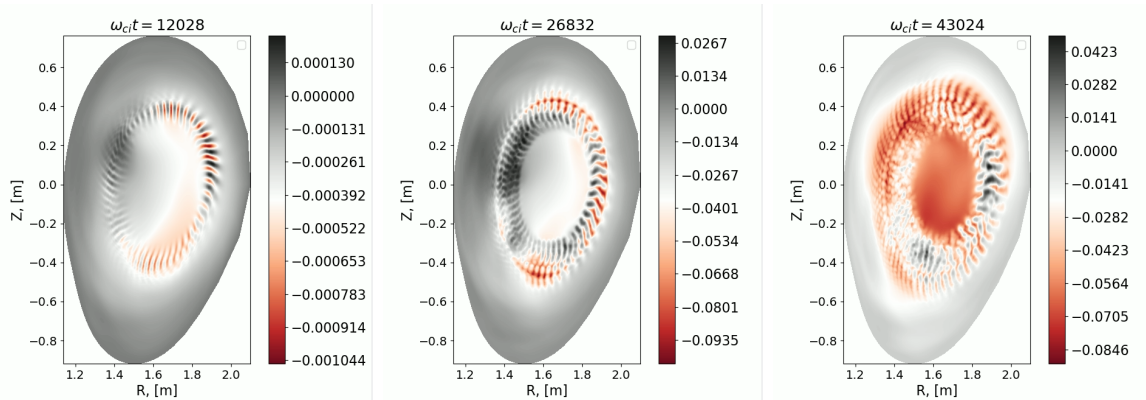

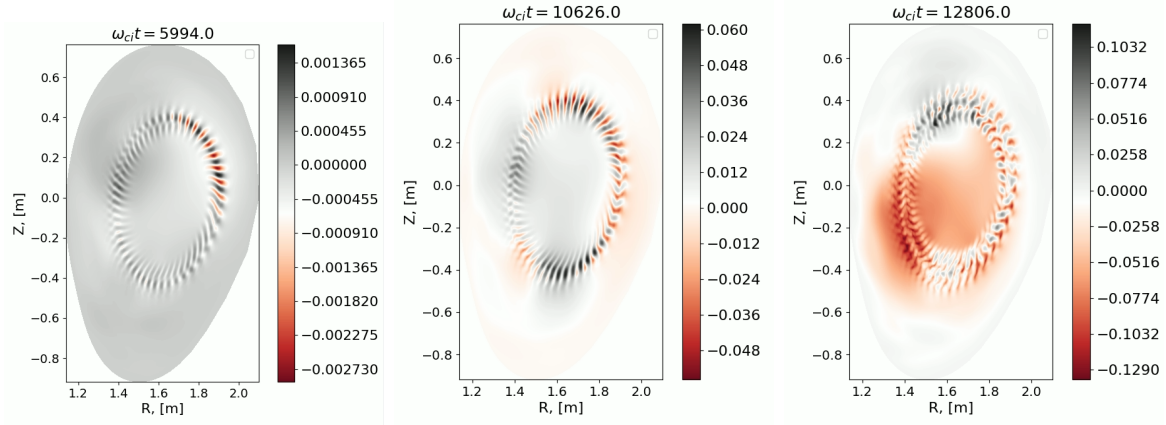**Figure 9.** Evolution of the electrostatic potential in ASDEX-Upgrade for the ITG regime, $\beta = 0.4\%$.

Figure 10. Evolution of the electrostatic potential in ASDEX-Upgrade for the KBM regime, $\beta = 4.8\%$.
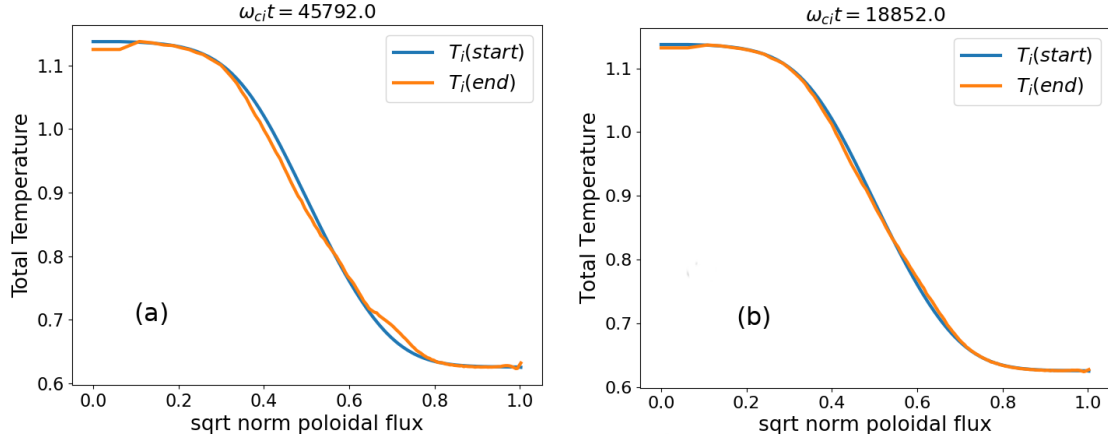

Figure 11. Temperature profile evolution in the ASDEX-Upgrade geometry in (a) the ITG regime, $\beta = 0.4\%$, and (b) the KBM regime, $\beta = 4.8\%$. One sees that the profiles do not change much in contrast to the more unstable circular-geometry case.
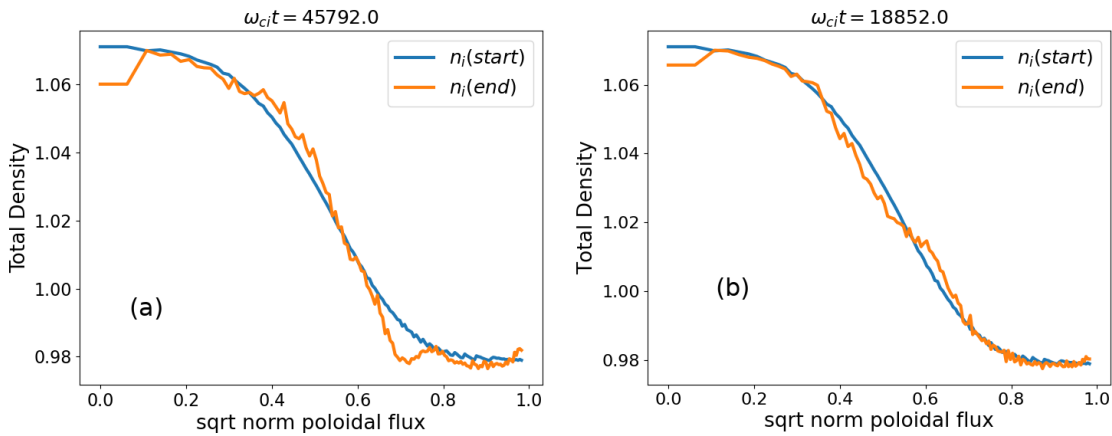

Figure 12. Density profile evolution for (a) the ITG regime, $\beta = 0.4\%$, and (b) the KBM regime, $\beta = 4.8\%$. One can see a density peaking (corresponding to an inward turbulent pinch) in the ITG regime. The particle flux in the KBM regime is outward.

Another interesting topic left for future studies is related to the coupling of the nonlinear KBM dynamics with reconnection. It is known that the violation of the magnetic surfaces is possible for nonlinear evolution of both the electromagnetic ITG and the KBM instabilities. This is made possible by the parity mixing in the nonlinear regime [9] which may lead to reconnection events on various scales caused by the electromagnetic turbulence. In Ref. [11], it has been found that the KBM evolution is accompanied with a rapid growth of localized current sheets excited by the nonlinear ponderomotive force saturating kinetically at the spatial scales comparable to the ion gyro-radius. In this paper, we make the first step using ORB5 in this direction coupling the nonlinear tearing instability and electromagnetic turbulence in Section 3.

Finally, there is an ongoing work [25, 26, 27] related to the strong reduction of turbulent heat fluxes at finite beta [7] for certain parameters observed in some experiments [27]. In this Section, our goal is to demonstrate that, despite the cancellation problem, global nonlinear simulations of electromagnetic turbulence are possible both in the ITG and the KBM regimes using the fully-gyrokinetic particle-in-cell approach. This represents the first necessary step before combining the turbulence with other global gyrokinetic phenomena such as the MHD-like events, Alfvén Eigenmodes, or fast particles. In Section 4, we consider an example of an Alfvén Eigenmode destabilized by the fast particles and evolving in presence of the electromagnetic turbulence.

3. Tearing instability and electromagnetic turbulence

The impact of magnetic islands on plasma confinement depends on several parameters such as their spatial distribution, frequency or size which can range from a millimeter to a fraction of the plasma radial extent [28, 29, 30, 15, 22]. It was shown numerically that an island size can reach 20% of ITER small radius without applied counter-measures [31]. Such a large island can dramatically degrade the confinement in ITER [32]. While the evolution and saturation of finite-size magnetic islands is to a large extent understood and can be modeled quite reliably in experiments, the physics governing their seeding and their initial stability is fairly complex and a disentanglement of the various possible effects is difficult. A particularly interesting gyrokinetics result is the possibility that turbulence triggers magnetic islands [33], being at the origin of their growth. Magnetic islands also impact turbulence which is reduced inside the island as large-scale flows are expelled from it and turbulence develops mostly around the reconnection region ('X'-point) [22]. At the same time, large-scale vortex flows are observed in simulations to develop inside wide magnetic islands [30, 15]. In this Section, we demonstrate capabilities of ORB5 to simulate nonlinear tearing instabilities alone and also in presence of the electromagentic turbulence.

We consider a tokamak with circular cross-sections, the aspect ratio $A = 10$, the machine size $L_x = 200$, and the safety factor [33, 34]:

$$q = q_{\mathrm{a}} \frac{\rho^2/r_{\mathrm{a}}^2}{1 - (1 - \rho^2/r_{\mathrm{a}}^2)^2} \tag{3}$$
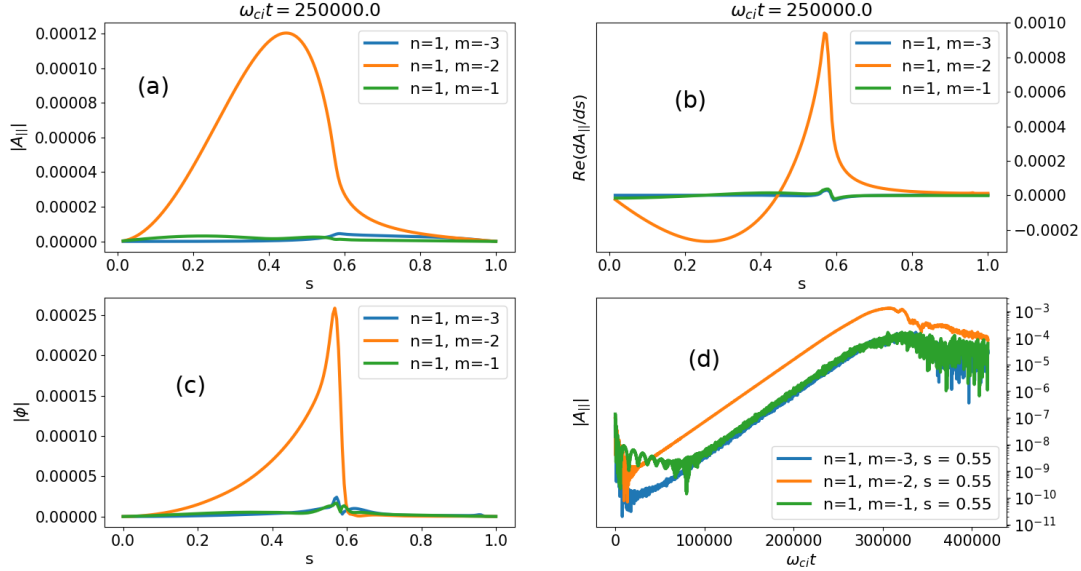
Figure 13. Nonlinear tearing mode. (a) The parallel magnetic potential has a typical structure of the tearing mode instability. (b) The radial derivative of the parallel magnetic potential which is closely related to the tearing instability parameter Δ'. It has a distinct spike at the resonant flux surface. (c) The electrostatic potential has a maximum at the resonant flux surface. It's structure is typical for the tearing mode instability. (d) The temporal evolution of the parallel magnetic potential at the $s = 0.55$ flux surface. The mode clearly enters the nonlinear phase with the tearing Fourier harmonic $n = 1$, $m = -2$ being dominant.

with ρ the radial coordinate, r_a the minor radius, and $q_a = 3.5$. This safety factor profile has a $q = 2$ resonance at $s = 0.58$ and is unstable with respect to the tearing mode. In gyrokinetic simulations, the tearing instability drive is included via the shifted Maxwellian distribution function for the electrons with the parallel-velocity shift determined by the ambient parallel current, similar to Ref. [33].

In Fig. 13(d), the evolution of the tearing instability is shown for the parallel magnetic potential at the $s = 0.55$ flux surface. One sees that the mode enters the nonlinear phase. The simulation is quite expensive computationally because of a relatively low growth rate of the collisionless tearing instability and the physical importance of the collisionless electron skin depth which is resolved in the simulations. The reduced mass ratio $m_i/m_e = 200$ and $\beta = 0.4\%$ are used. The mode considered in Fig. 13 is driven only by the profile of the ambient parallel current. The plasma temperature and density profiles are flat. The total number of the ion markers is $N_i = 400\,000\,000$ and the total number of the electron markers is $N_e = 400\,000\,000$. We have used 307 grid points in the radial direction, 384 grid points in the poloidal direction, and 128 grid points in the toroidal direction. The Fourier filter has been applied with the mode numbers $-30 \leq n \leq 30$ kept in the toroidal filter. For the poloidal modes, the diagonal filter has been used with the width of 11 modes centered
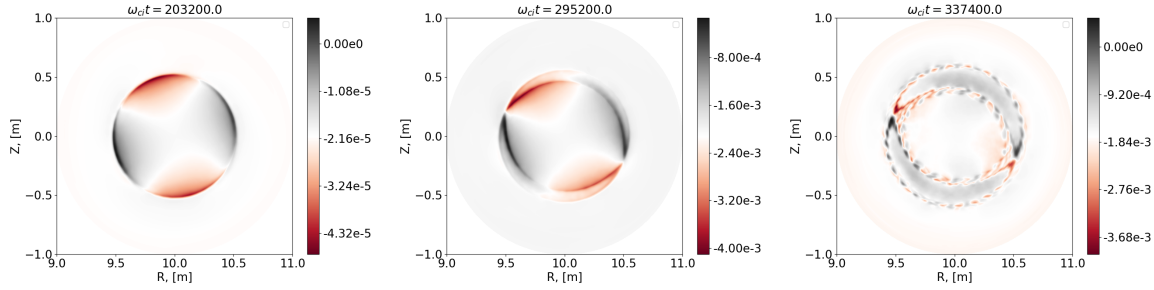
Figure 14. Evolution of the electrostatic potential in tokamak plasmas during the collisionless tearing instability. Flat plasma temperature and density are considered. One sees how an island develops in time with the X-points clearly visible.

at the resonant poloidal mode number satisfying the condition $m_{res} = q(s)n$ for a given toroidal mode number n at a given flux surface s. The time step $\Delta t = 5\,\omega_{ci}^{-1}$ has been used. The Krook operator is not applied. The simulation duration is about 10 days (one day is 24 hours) on 128 nodes of Marconi (48 Intel SKL cores per node). Using the realistic mass ratio, it would require several times reduction in the time step and increase in the radial resolution to resolve the skin depth which is decreasing with the square root of the electron mass. This would make the simulation duration longer than a month. The snapshots of the $n = 1$ harmonic of the perturbation are shown in Fig. 13 for the linear stage at $\omega_{ci}t = 0.25 \times 10^6$: (a) the parallel magnetic potential and (c) the electrostatic potential. One sees that a typical tearing mode structure has developed. In Fig. 13(b), the radial derivative of the parallel magnetic potential is plotted. This quantity is closely related to the tearing instability parameter Δ'. As expected, it has a sharp maximum at the resonant flux surface.

In Fig. 14, the evolution of the electrostatic potential is shown in the poloidal cross-section which includes all Fourier harmonics. One can see the tearing mode linearly excited and growing into the nonlinear island structure. The X-points are clearly visible in the nonlinear stage. For comparison, the mode evolution is shown in the case of finite temperature and density gradients in Fig. 15. Here, the plasma profiles are given by Eqs. (1) and (2) with $s_0 = 0.5$, $\kappa_n = 0.1$, $\kappa_T = 0.5$, and $\Delta_T = \Delta_n = 0.2$. One sees that the tearing instability develops also in this case. The snapshots of the electrostatic potential are plotted in Fig. 16 showing the microturbulence developing in addition to the tearing mode. Note that the marker weights have been initialized using only the tearing toroidal $n = 1$ and poloidal $m = -2$ mode numbers. This particular initialization leads to an excitation and dominance of the tearing instability in the first phase of the simulations. At the later stage, a global mode, possibly of an Alfvénic nature, appears. We will study this case in detail in our future work. Here, we just note that it could give an example of a self-consistent combination of the MHD tearing instability, microturbulence, and, eventually, an Alfvénic mode and a zonal flow. Such interlinked physical systems [35] can be addressed only within a global nonlinear framework and represent the main target of our work.
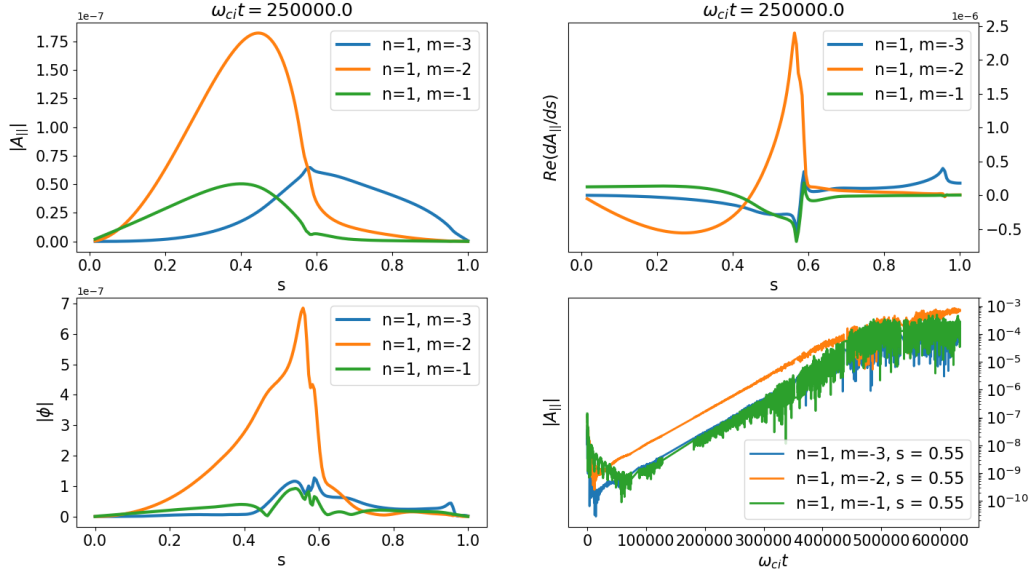
Figure 15. Nonlinear tearing mode in presence of the temperature and density gradients. (a) The parallel magnetic potential has a typical structure of the tearing mode instability. (b) The radial derivative of the parallel magnetic potential. (c) The electrostatic potential has a maximum at the resonant flux surface. (d) The temporal evolution of the parallel magnetic potential at the $s = 0.55$ flux surface. We have experienced problems with data transfer between different filesystems on the supercomputer at several restarts of the simulation. This led to loss of a small faction of data in the linear phase which can be seen in this figure (e. g. around $\omega_{ci} \sim 140\,000$).
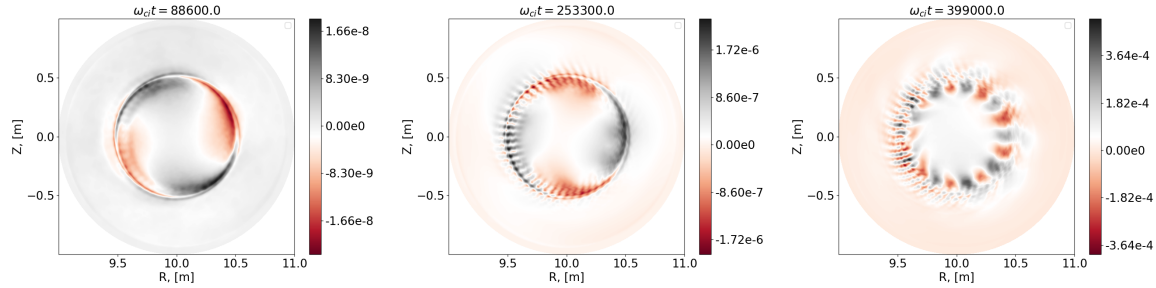

Figure 16. Evolution of the electrostatic potential in tearing-unstable tokamak plasma with finite temperature and density gradients. One sees that the microturbulence is excited in addition to the tearing component. Also, a global mode, possibly of an Alfvénic nature, is excited at later times.
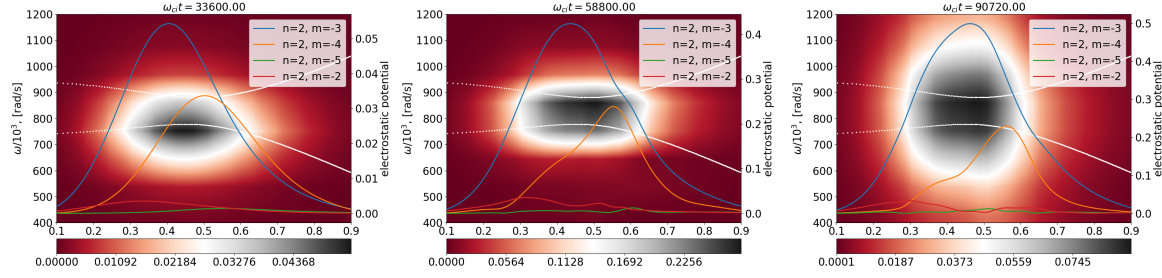
Figure 17. Evolution of the TAE $n = 2$ frequency for the case of flat bulk plasma temperature. Here, the windowed Fourier transform of the electrostatic potential is shown for the toroidal mode number $n = 2$ and the poloidal mode numbers $-5 \leq m \leq -2$. One sees that the frequency of the mode remains at the toroidicity-induced gap. The shear Alfvén continuum (the white lines on the plot) is computed using the slow-sound approximation.
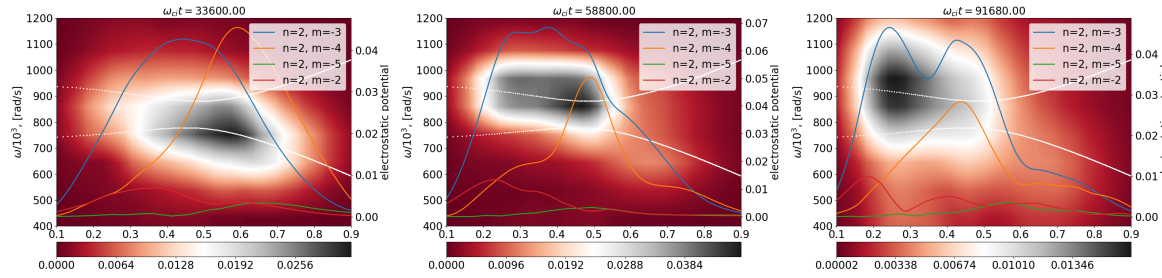

Figure 18. Simulations using the same parameters as in Fig. 17 except the bulk-plasma temperature which has now a weak gradient $\kappa_{\mathrm{T}} = 0.4$, see Eq. (4). One sees that the frequency evolves along the continuum branch. The same quantity is shown as in Fig. 17 (the Fourier transform of the electrostatic potential). The shear Alfvén continuum is shown with the white lines.

4. Alfvén Eigenmodes in the presence of fast ions and electromagnetic turbulence

In this Section, we address the issue of coupling between the turbulence and Alfvén Eigenmodes destabilized by the fast ions. While a considerable amount of research has been devoted to the interaction of Alfvén Eigenmodes and fast ions [36], little is known about the role that turbulence may - or may not - have on the nonlinear behaviour of Alfvén Eigenmodes. Recent works have focused on the interaction of AEs and zonal structures [16], showing a complex behaviour. In Ref. [37], it has been suggested that the microturbulence interaction with energetic particles can be a key factor determining the regime of the mode saturation (quasi-steady or chirping) with far-reaching consequences for the energetic-particle transport (although a direct transport of the energetic particles by the microturbulence is normally small). In Ref. [38], a nonlinear damping of Alfvén
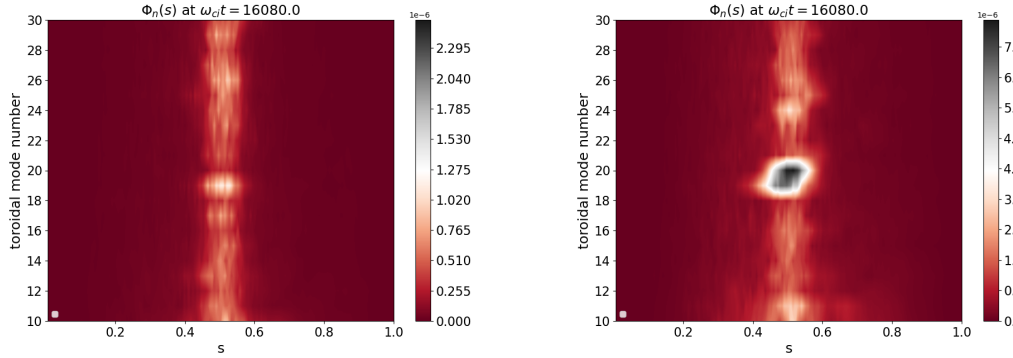
Figure 19. Electrostatic potential plotted as a function of the flux surface label s and the toroidal mode number n. Only the relevant part of the spectrum is shown. One sees that there is a mode activity in the case with the finite temperature gradient (b). In contrast, the case of the flat temperature gradient (a) does not have the mode activity. A consequence of the mode activity in (b) is a higher amplitude of the perturbation in the nonlinear phase which can be related to the characteristic frequency evolution observed in Fig. 18.
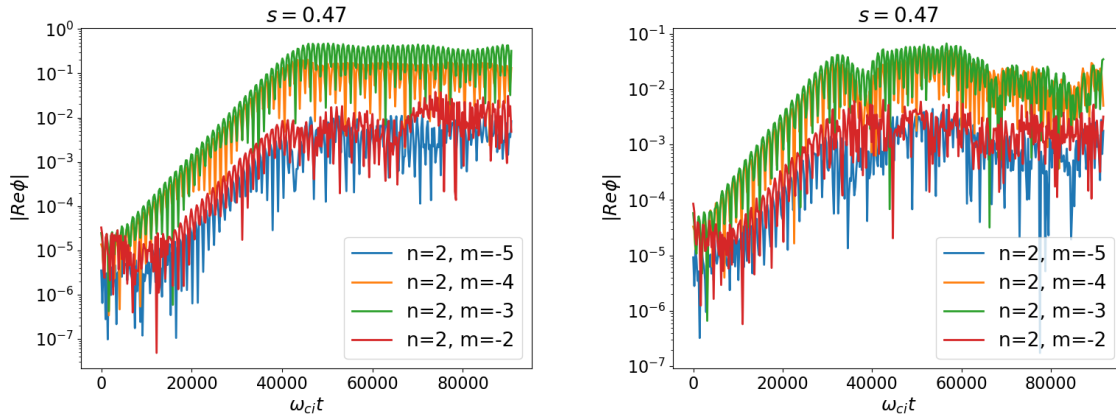

Figure 20. Evolution of $n = 2$ toroidal mode (TAE) for (a) flat bulk plasma profiles and (b) finite bulk-plasma temperature gradient (see the main text for details).

Eigenmodes caused by their scattering on microturbulence via generation of short-wavelength electron Landau damped kinetic Alfvén waves has been considered. On the other hand, there is an ongoing work [25, 26, 27] addressing effects of the energetic particles and Alfvénic modes on the turbulence. This all calls for a computational effort coupling the global electromagentic turbulence, Alfvénic dynamics, and fast-particle destabilization, which is the focus of this Section.

Here, in order to find out whether the presence of turbulence affects the Alfvén Eigenmode evolution, we shall consider two cases: one in which bulk plasma gradients are zero and therefore no bulk turbulence is present, and the other case with finite bulk plasma gradients in which turbulence is present. We consider a circular cross-section tokamak with the aspect ratio $A = 10$ and the machine size $L_x = 350$. The

magnetic geometry is that of the ITPA benchmark [39, 40]. All particle species (bulk ions, electrons, and fast ions) are kinetic and nonlinear. The reduced mass ratio $m_i/m_e = 200$ and $\beta = 1.72\%$ are used. For the fast particles, Deuterium ions are selected with the temperature $T_f/T_i = 40$ and the density $n_f/n_i = 0.005$. Here, T_i is the bulk-ion temperature and n_i is the bulk-ion density. The Maxwell distribution function is chosen for the fast ions. The fast-ion temperature profile is flat, the fast-ion density profile is given by Eq. (1) with $\kappa_n = 3.33$, $s_0 = 0.5$, and $\Delta_n = 0.2$. The total number of the ion markers $N_i = 400\,000\,000$ and the total number of the electron markers is $N_e = 400\,000\,000$. We have used 160 grid points in the radial direction, 384 grid points in the poloidal direction, and 192 grid points in the toroidal direction. The Fourier filter has been applied with the mode numbers $-40 \le n \le 40$ kept in the toroidal filter. For the poloidal modes, the diagonal filter has been used with the width of 11 modes centered at the resonant poloidal mode number satisfying the condition $m_{res} = q(s)n$ for a given toroidal mode number n at a given flux surface s. The time step $\Delta t = 3\,\omega_{ci}^{-1}$ has been used. The Krook operator with the decay rate $\gamma_K = 1.5 \times 10^{-4}\omega_{ci}$ is applied for the ions and the electrons. The simulation duration is several days (one day is 24 hours) on 64 nodes of Marconi100 (4 NVIDIA Volta V100 GPUs and 4 MPI tasks per node, 32 CPU cores per MPI task). For the realistic mass ratio, the simulation would take several times longer because of the time step which is inversely proportional to the square root of the mass ratio.

In Fig. 17, the frequency evolution is shown for the case of a flat bulk-ion profile for the toroidal Fourier harmonic $n = 2$. It corresponds to the dominant TAE instability for the parameters considered. There are other TAEs, for example at the toroidal mode number $n = 6$, which are however less unstable. One can see that the frequency remains at the toroidicity-induced gap for all times of the nonlinear evolution. The shear-Alfvén continuum is computed using the CONTI code [41, 42] within the slow-sound approximation.

In contrast, the frequency of the same TAE evolves along the continuum branch when the bulk-plasma species have a temperature gradient, see Fig. 18. Here, we apply a rather shallow bulk-plasma temperature profile given by the expression:

$$T_{0s}(\rho)/T_{0s}(\rho_0) = \exp\left[-\frac{\kappa_T \Delta_T}{2}\ln\left[\frac{\cosh\left(\frac{\rho-\rho_0+\Delta\rho}{\Delta_T}\right)}{\cosh\left(\frac{\rho-\rho_0-\Delta\rho}{\Delta_T}\right)}\right]\right] \tag{4}$$

with ρ the minor radius, $\kappa_T = 0.4$, $\Delta_T = 0.04$, $\rho_0 = 0.5$, and $\Delta\rho = 0.4$. All other physical and computational parameters remain unchanged. Note that the white lines on Figs. 17 and 18 correspond to the shear Alfvén continuum plotted for the toroidal mode number $n = 2$. Despite the inevitable inaccuracies naturally associated with frequency analysis of nonlinear data, one can see that the frequency evolution (computed using the windowed Fourier approach) is very different on the both Figures. The light spot indicating the mode frequency and its location does not move radially in the absence of the bulk-plasma temperature gradient, Fig. 17, althouth its width in the

frequency increases. The mode remains centered at the TAE gap both radially and in the frequency. In contrast, the light spot moves radially inward in Fig. 18 where the bulk-plasma temperature gradient is finite. Its frequency (the center of the light spot) roughly follows the upper branch of the shear Alfvén continuum (the upper white line) during the inward radial motion. A dynamics of such type is characteristic for the chirping phenomena [43, 44, 45, 46, 47]. The nonlinear evolution of Alfvénic instabilities driven by the fast particles results in flattening of the fast-particle density at the resonance location and its steepening at the adjacent radii. The chirping modes are capable to tune their frequency so that the new resonant location shifts to the current position of the maximal gradient further driving the instability. This process is accompanied by changes in the radial location of the mode, as can be seen in Fig. 18. The instability with the frequency following the continuum branch can be identified as an Energetic Particle Mode (EPM): this type of mode is known to be destabilized if the energetic particle drive is strong enough and, unlike the TAE, does not have an equivalent in the ideal MHD limit. The chirping EPM nonlinear dynamics (see e.g. the recent studies of Refs. [45, 47]) can be such that it is seen to move radially inwards, following a continuum branch. This results in a upward or downward frequency chirping, depending on which continuum branch is concerned. Our results are therefore consistent with an upward-chirping EPM.

 A possible cause for the frequency evolution in this case can be higher amplitudes of the Fourier harmonics corresponding to the drift instabilities. An indication for such instabilities excited by the temperature profile considered can be seen in Fig. 19. Here, the elecrostatic potential is plotted as a function of the flux surface label and the toroidal mode number. One can see a coherent instability developing at $n \approx 20$ when the bulk-plasma temperature has a gradient. Note that that this physically unstable mode is clearly separated from the filter boundaries indicating a sufficient resolution. It was important to choose a finite but low level of the microturbulence drive (i. e. shallow bulk-plasma profiles) to obtain the chirping Alfvénic instability, in agreement with Ref. [37]. In Fig. 20, we compare the temporal evolution of the instability with and without the bulk-plasma temperature gradient selecting the toroidal mode number $n = 2$ and plotting the temporal evolution of the respective dominant poloidal harmonics. One sees that the evolution pattern becomes more complex in Fig. 20(b) when the bulk-plasma temperature gradient is finite. Clearly, more work needs to be done in future in order to fully understand the physical mechanism behind these observations.

5. Stellarator turbulence

Turbulence plays an important role in stellarators, particularly if the neoclassical losses have been reduced by optimization of the magnetic field [48]. Confinement has been studied in Wendelstein 7-X experiments [49, 50, 51, 52], and these have been accompanied by nonlinear gyrokinetic simulations, but most of the latter have been performed in a flux tube [53, 54, 10]. However, other than in an ideally axisymmetric tokamak, stellarator flux tubes are not equivalent to each other, there is no good
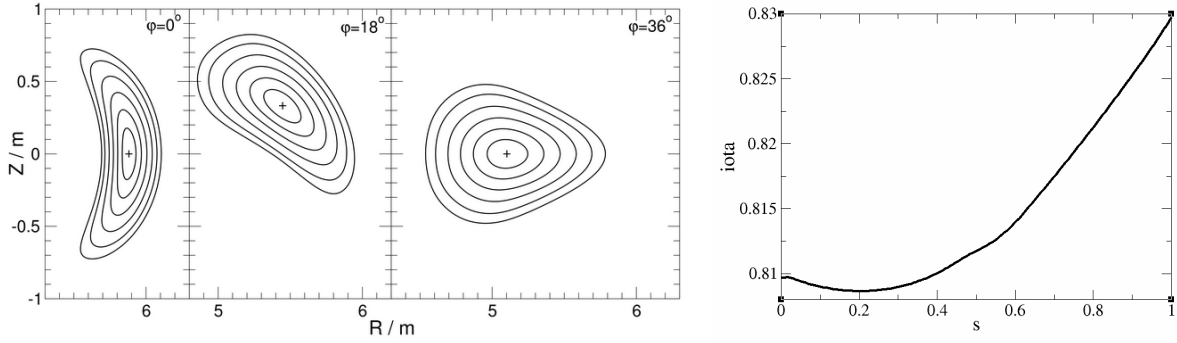
Figure 21. The characteristic cross-sections at several toroidal angles and the rotational transform (iota) of the W7-X configuration considered. The normalized toroidal flux s is used as the radial coordinate for the rotational transform.
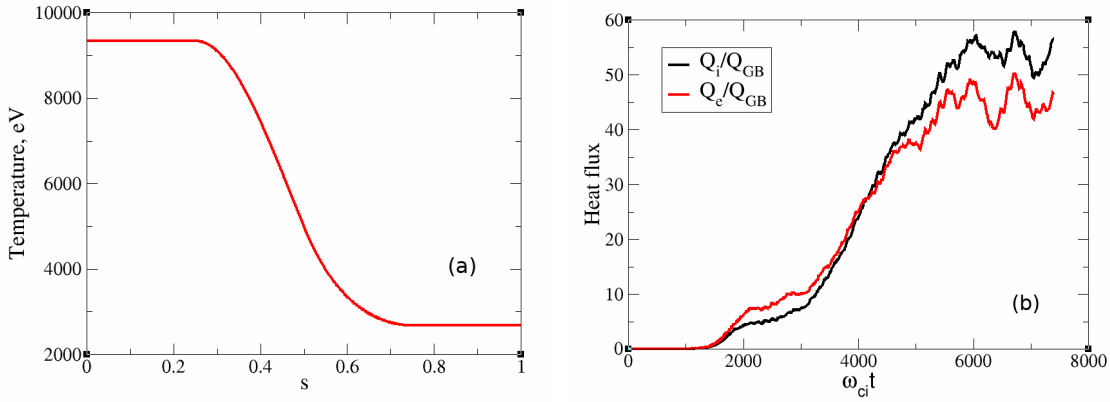

Figure 22. The plasma temperature (a) and the resulting turbulent heat flux (b) in W7-X. The normalized toroidal flux s is used as the radial coordinate.

way to incorporate the ambient radial electric field, and simulations of the Kinetic Ballooning Mode (KBM) turbulence can be problematic in a flux tube [10]. To resolve these issues, a global electromagnetic approach is needed. In Ref. [55], the GENE-3D code has been applied to Wendelstein 7-X with the goal of addressing electromagnetic stabilization of ITG turbulence. In this Section, we apply the EUTERPE code to study the electromagnetic turbulence in a stellarator plasma.

We consider a Wendelstein 7-X [51] configuration falling into the class of variants which exploit the rotational transform $\iota = 5/6$ and the corresponding edge islands for divertor operation. Furthermore, the specific case chosen here is characterized by a very high magnetic mirror field, on the magnetic axis $(B_{max} - B_{min})/(2 < B >) \approx 0.25$, which has to be compared to the magnetic mirror of 0.1 in the Wendelstein 7-X standard case. On the one hand, this magnetic mirror leads to a small bootstrap current, on the other hand, it prevents the formation of a vacuum-field magnetic well. In fact, this configuration even possesses a vacuum-field magnetic hill, which means that, when going from the magnetic axis to the plasma boundary, the enclosed volume grows more strongly than the enclosed magnetic flux. Ideal MHD theory shows that such magnetic
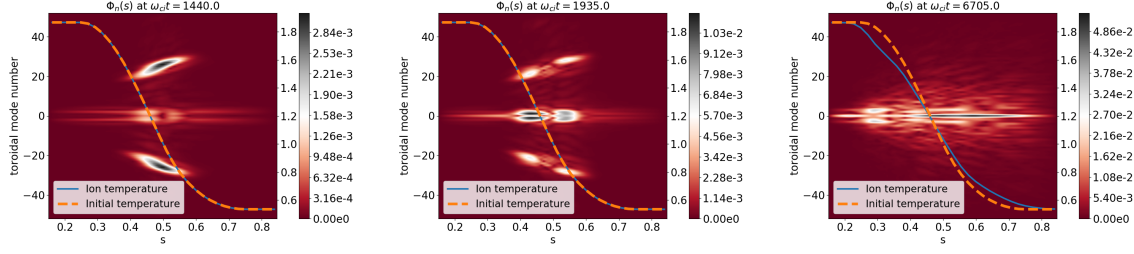
Figure 23. Evolution of the electrostatic potential in the W7-X as a function of the flux label and toroidal mode number. One can see how the linear instability evolves generating the low-mode-number components (including the zonal flows) and modifying the ambient temperature profile in the nonlinear phase.
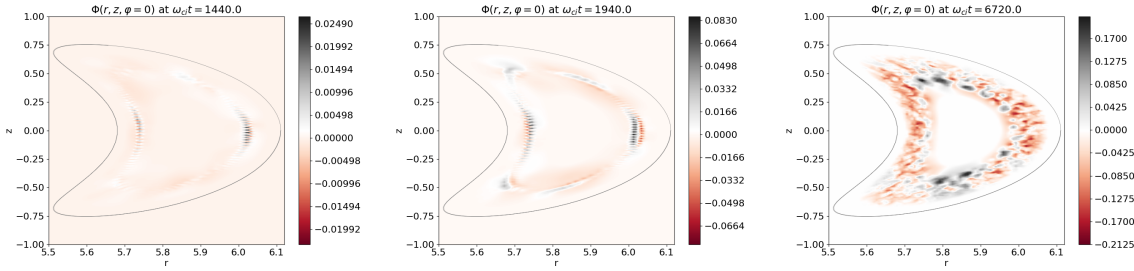

Figure 24. Evolution of electrostatic potential in the W7-X shown in the poloidal cross-section corresponding to the toroidal angle $\varphi = 0$.

configurations are plagued by the lack of ideal MHD stability. In Ref. [56], a similar W7-X variant was found to be unstable against low-mode-number ideal MHD modes at even low plasma pressure. In this paper, we consider the gyrokinetic modes developing nonlinearly in such MHD-unstable stellarator equilibria.

For the configuration studied here a free-boundary plasma equilibrium was computed using the ideal MHD equilibrium code VMEC [57]. For a plasma volume of $V_{\text{plasma}} = 25$ m^3, a uniform number density of $n_0 = 1.4 \times 10^{19}$ m^{-3} and the temperature profile shown in Fig. 22(a) correspond to $\beta = 1.52\%$ at the center of the simulation volume, i. e. at the normalized toroidal flux $s = 0.5$. The characteristic cross-sections illustrating the non-axisymmetric geometry of the stellarator and the rotational transform are shown in Fig. 21. The temperature profile is defined following Ref. [58]:

$$\frac{\mathrm{d}\ln T_{i,e}}{\mathrm{d}s} = \begin{cases} -20\left(\frac{1}{4} - \left|s - \frac{1}{2}\right|\right), & 0.25 \leq s \leq 0.75 \\ 0, & otherwise \end{cases} \tag{5}$$

Here, s is the normalized toroidal flux. The reduced mass ratio $m_i/m_e = 200$ is used. At the relatively low β considered here, the mode is the electromagnetic ITG. The total number of the ion markers is $N_i = 750\,000\,000$ and the total number of the electron markers is $N_e = 1\,000\,000\,000$. We have used 180 grid points in the radial direction, 1024 grid points in the poloidal direction, and 256 grid points in the toroidal

direction. The Fourier filter has been applied with the mode numbers $-60 \leq n \leq 60$ kept in the toroidal filter. For the poloidal modes, the diagonal filter has been used with the width of 35 modes centered at the resonant poloidal mode number satisfying the condition $m_{res} = q(s)n$ for a given toroidal mode number n at a given flux surface s. The time step $\Delta t = 0.5\,\omega_{ci}^{-1}$ has been used. The Krook operator with the decay rate $\gamma_K = 10^{-4}\omega_{ci}$ is applied for the both species. The simulations are carried out in the annulus $0.15 \leq s \leq 0.85$ with the Dirichlet boundary conditions employed on the both sides. A single period of the magnetic configuration is considered (there are five periods in Wendelstein 7-X). The simulation duration is about 20 days (one day is 24 hours) on 128 nodes of Marconi (48 Intel SKL cores per node). This is the most expensive simulation in this paper. It would take several times longer (months) for the realistic mass ration because of the time step inversely proportional to the square root of the mass ratio. The resulting turbulent evolution of the heat flux is shown in Fig. 22(b). Here, the radial heat flux is calculated as an average over the whole simulation domain. One can see that the simulation clearly enters the nonlinear phase.

The electrostatic potential at different times is shown in Fig. 23 as a function of the flux surface label and the toroidal mode number. Here, one can see that a linear instability develops at early times. The low-mode-number part of the spectrum (which includes the zonal flow) is excited when the turbulence evolves. At later times, the temperature profile is modified via the turbulent relaxation. In Fig. 24, the electrostatic potential is shown in the poloidal cross-section corresponding to the toroidal angle $\varphi = 0$. One sees that the perturbation covers only a small fraction of the poloidal angles in the linear regime. It spreads over the whole poloidal domain in the nonlinear phase. In future, we will study global electromagnetic turbulence in stellarator plasma in detail.

6. Conclusions

In this paper, we have considered the electromagnetic turbulence in tokamak plasmas. The ITG-KBM transition has been identified and a strong relaxation of the profiles in the case of the KBM turbulence has been observed for the large-aspect-ratio tokamak. In this case, the mode saturation appears to be due to the flattening of the temperature profile caused by an outward transport of the turbulent finger-like structures. We have considered the electromagnetic turbulence in a down-scaled ASDEX-Upgrade plasma where a similar ITG-KBM transition has been observed as well. The profile relaxation is weaker in the ASDEX-Upgrade for the parameters considered. The multiscale physics has been addressed coupling the electromagnetic turbulence to the collisionless tearing instability and Alfvénic modes destabilized by the fast ions. Electromagnetic turbulence has also been addressed in the non-axisymmetric stellarator geometry.

A typical computational effort for the cases considered here requires large jobs on Marconi (128 nodes for many days of the simulation duration) or Marconi100 (64 nodes). In future, exascale computing systems will be needed for the reactor-size turbulence simulations and for massive parameter scans using the global codes. The

spatial resolution can also become an issue when the collisionless reconnection is of importance requiring the collisioneless electron skin depth to be resolved. Extending the simulations to the realistic mass ratio does not normally pose a problem. Of course, such simulations are computationally more expensive because of a smaller time step needed. This is the main reason to use a reduced mass ratio throughout this paper. A number of simulations at the realistic mass ratio has also been performed for various scenarios and will be reported elsewhere. Since the collisionless electron skin depth is affected when the electron mass is decreased, the radial resolution requirements can become more challenging for the realistic mass ratio when the tearing mode is present.

The main goal of this paper has been to present a set of the characteristic physics applications which can be used as a starting point for future more detailed numerical experiments with ORB5 and EUTERPE. Here, we demonstrate that the simulations of such kind are possible using existing global gyrokinetic particle-in-cell codes on the available HPC systems.

Acknowledgments

References

[1] Y. Chen and S. Parker, "Gyrokinetic turbulence simulations with kinetic electrons," *Physics of Plasmas*, vol. 8, no. 5, pp. 2095–2100, 2001. [Online]. Available: https://doi.org/10.1063/1.1351828

[2] A. Mishchenko, A. Bottino, R. Hatzky, E. Sonnendrücker, R. Kleiber, and A. Könies, "Mitigation of the cancellation problem in the gyrokinetic particle-in-cell simulations of global electromagnetic modes," *Physics of Plasmas*, vol. 24, no. 8, p. 081206, 2017. [Online]. Available: https://doi.org/10.1063/1.4997540

[3] E. Lanti, N. Ohana, N. Tronko, T. Hayward-Schneider, A. Bottino, B. McMillan, A. Mishchenko, A. Scheinberg, A. Biancalani, P. Angelino, S. Brunner, J. Dominski, P. Donnel, C. Gheller, R. Hatzky, A. Jocksch, S. Jolliet, Z. Lu, J. Martin Collar, I. Novikau, E. Sonnendrücker, T. Vernay, and L. Villard, "ORB5: A global electromagnetic gyrokinetic code using the PIC approach in toroidal geometry," *Computer Physics Communications*, vol. 251, p. 107072, 2020. [Online]. Available: http://www.sciencedirect.com/science/article/pii/S0010465519303911

[4] V. Kornilov, R. Kleiber, R. Hatzky, L. Villard, and G. Jost, "Gyrokinetic global three-dimensional

simulations of linear ion-temperature-gradient modes in Wendelstein 7-X," *Physics of Plasmas*, vol. 11, no. 6, pp. 3196–3202, 2004. [Online]. Available: https://doi.org/10.1063/1.1737393

[5] A. Mishchenko, A. Biancalani, A. Bottino, T. Hayward-Schneider, P. Lauber, E. Lanti, L. Villard, R. Kleiber, A. Könies, and M. Borchardt, "Numerics and computation in gyrokinetic simulations of electromagnetic turbulence with global particle-in-cell codes," *Plasma Physics and Controlled Fusion*, vol. 63, no. 8, p. 084007, jun 2021. [Online]. Available: https://doi.org/10.1088/1361-6587/ac0bcb

[6] M. J. Pueschel, M. Kammerer, and F. Jenko, "Gyrokinetic turbulence simulations at high plasma beta," *Physics of Plasmas*, vol. 15, no. 10, p. 102310, 2008. [Online]. Available: https://doi.org/10.1063/1.3005380

[7] M. J. Pueschel and F. Jenko, "Transport properties of finite-beta microturbulence," *Physics of Plasmas*, vol. 17, no. 6, p. 062307, 2010. [Online]. Available: https://doi.org/10.1063/1.3435280

[8] S. Maeyama, A. Ishizawa, T.-H. Watanabe, M. Nakata, N. Miyato, M. Yagi, and Y. Idomura, "Comparison between kinetic-ballooning-mode-driven turbulence and ion-temperature-gradient-driven turbulence," *Physics of Plasmas*, vol. 21, no. 5, p. 052301, 2014. [Online]. Available: https://doi.org/10.1063/1.4873379

[9] A. Ishizawa, S. Maeyama, T.-H. Watanabe, H. Sugama, and N. Nakajima, "Electromagnetic gyrokinetic simulation of turbulence in torus plasmas," *Journal of Plasma Physics*, vol. 81, no. 2, p. 435810203, 2015.

[10] K. Aleynikova, A. Zocco, P. Xanthopoulos, P. Helander, and C. Nührenberg, "Kinetic ballooning modes in tokamaks and stellarators," *Journal of Plasma Physics*, vol. 84, no. 6, p. 745840602, 2018. [Online]. Available: https://doi.org/10.1017/S0022377818001186

[11] G. Dong, J. Bao, A. Bhattacharjee, and Z. Lin, "Nonlinear saturation of kinetic ballooning modes by zonal fields in toroidal plasmas," *Physics of Plasmas*, vol. 26, no. 1, p. 010701, 2019. [Online]. Available: https://doi.org/10.1063/1.5066583

[12] A. Ishizawa, K. Imadera, Y. Nakamura, and Y. Kishimoto, "Global gyrokinetic simulation of turbulence driven by kinetic ballooning mode," *Physics of Plasmas*, vol. 26, no. 8, p. 082301, 2019. [Online]. Available: https://doi.org/10.1063/1.5100308

[13] N. Kumar, Y. Camenen, S. Benkadda, C. Bourdelle, A. Loarte, A. Polevoi, F. Widmer, and JET contributors, "Turbulent transport driven by kinetic ballooning modes in the inner core of JET hybrid H-modes," *Nuclear Fusion*, vol. 61, no. 3, p. 036005, 2021. [Online]. Available: https://doi.org/10.1088/1741-4326/abd09c

[14] M. J. Pueschel, D. R. Hatch, T. Görler, W. M. Nevins, F. Jenko, P. W. Terry, and D. Told, "Properties of high-β microturbulence and the non-zonal transition," *Physics of Plasmas*, vol. 20, no. 10, p. 102301, 2013. [Online]. Available: https://doi.org/10.1063/1.4823717

[15] M. J. Pueschel, P. W. Terry, F. Jenko, D. R. Hatch, W. M. Nevins, T. Görler, and D. Told, "Extreme heat fluxes in gyrokinetic simulations: A new critical β," *Phys. Rev. Lett.*, vol. 110, p. 155005, Apr 2013. [Online]. Available: https://link.aps.org/doi/10.1103/PhysRevLett.110.155005

[16] A. Biancalani, A. Bottino, P. Lauber, A. Mishchenko, and F. Vannini, "Effect of the electron redistribution on the nonlinear saturation of Alfvén eigenmodes and the excitation of zonal flows," *Journal of Plasma Physics*, vol. 86, no. 3, p. 825860301, 2020.

[17] S. C. Cowley and M. Artun, "Explosive instabilities and detonation in magnetohydrodynamics," *Physics Reports*, vol. 283, no. 1, pp. 185–211, 1997, turbulence and Intermittency in Plasmas. [Online]. Available: https://www.sciencedirect.com/science/article/pii/S0370157396000609

[18] O. A. Hurricane, B. H. Fong, S. C. Cowley, F. V. Coroniti, C. F. Kennel, and R. Pellat, "Substorm detonation," *Journal of Geophysical Research: Space Physics*, vol. 104, no. A5, pp. 10 221–10 231, 1999. [Online]. Available: https://agupubs.onlinelibrary.wiley.com/doi/abs/10.1029/1999JA900012

[19] M. D. J. Cole, R. Hager, T. Moritaka, J. Dominski, R. Kleiber, S. Ku, S. Lazerson, J. Riemann, and C. S. Chang, "Verification of the global gyrokinetic stellarator code xgc-s for linear ion

temperature gradient driven modes," *Physics of Plasmas*, vol. 26, no. 8, p. 082501, 2019. [Online]. Available: https://doi.org/10.1063/1.5109259

[20] C. Ma and X. Xu, "Global kinetic ballooning mode simulations in BOUT++," *Nuclear Fusion*, vol. 57, no. 1, p. 016002, sep 2016. [Online]. Available: https://doi.org/10.1088/0029-5515/57/1/016002

[21] F. Vannini, A. Biancalani, A. Bottino, T. Hayward-Schneider, P. Lauber, A. Mishchenko, E. Poli, and G. Vlad, "Gyrokinetic investigation of the nonlinear interaction of Alfvén instabilities and energetic particle-driven geodesic acoustic modes," *Physics of Plasmas*, vol. 28, no. 7, p. 072504, 2021. [Online]. Available: https://doi.org/10.1063/5.0049588

[22] A. Ishizawa, Y. Kishimoto, and Y. Nakamura, "Multi-scale interactions between turbulence and magnetic islands and parity mixture—a review," *Plasma Physics and Controlled Fusion*, vol. 61, no. 5, p. 054006, mar 2019. [Online]. Available: https://doi.org/10.1088/1361-6587/ab06a8

[23] C. Angioni, E. Fable, M. Greenwald, M. Maslov, A. G. Peeters, H. Takenaga, and H. Weisen, "Particle transport in tokamak plasmas, theory and experiment," *Plasma Physics and Controlled Fusion*, vol. 51, no. 12, p. 124017, nov 2009. [Online]. Available: https://doi.org/10.1088/0741-3335/51/12/124017

[24] A. Mishchenko, P. Helander, and Y. Turkin, "Curvature particle pinch in tokamak and stellarator geometry," *Physics of Plasmas*, vol. 14, no. 10, p. 102308, 2007. [Online]. Available: https://doi.org/10.1063/1.2789988

[25] A. D. Siena, T. Görler, H. Doerk, E. Poli, and R. Bilato, "Fast-ion stabilization of tokamak plasma turbulence," *Nuclear Fusion*, vol. 58, no. 5, p. 054002, mar 2018. [Online]. Available: https://doi.org/10.1088/1741-4326/aaaf26

[26] A. D. Siena, T. Görler, E. Poli, A. B. Navarro, A. Biancalani, and F. Jenko, "Electromagnetic turbulence suppression by energetic particle driven modes," *Nuclear Fusion*, vol. 59, no. 12, p. 124001, sep 2019. [Online]. Available: https://doi.org/10.1088/1741-4326/ab4088

[27] S. Mazzi, J. Garcia, D. Zarzoso, Y. O. Kazakov, J. Ongena, M. Dreval, M. Nocente, Ž. Štancar, G. Szepesi, J. Eriksson, A. Sahlberg, S. Benkadda, and J. Contributors, "Enhanced performance in fusion plasmas through turbulence suppression by megaelectronvolt ions," *Nature Physics*, vol. 18, no. 7, pp. 776–782, Jul 2022. [Online]. Available: https://doi.org/10.1038/s41567-022-01626-8

[28] R. D. Hazeltine, D. Dobrott, and T. S. Wang, "Kinetic theory of tearing instability," *The Physics of Fluids*, vol. 18, no. 12, pp. 1778–1786, 1975. [Online]. Available: https://aip.scitation.org/doi/abs/10.1063/1.861097

[29] J. F. Drake and Y. C. Lee, "Kinetic theory of tearing instabilities," *The Physics of Fluids*, vol. 20, no. 8, pp. 1341–1353, 1977. [Online]. Available: https://aip.scitation.org/doi/abs/10.1063/1.862017

[30] W. A. Hornsby, A. G. Peeters, A. P. Snodin, F. J. Casson, Y. Camenen, G. Szepesi, M. Siccinio, and E. Poli, "The nonlinear coupling between gyroradius scale turbulence and mesoscale magnetic islands in fusion plasmas," *Physics of Plasmas*, vol. 17, no. 9, p. 092301, 2010. [Online]. Available: https://doi.org/10.1063/1.3467502

[31] F. Widmer, P. Maget, O. Février, H. Lütjens, and X. Garbet, "Non-linear simulations of neoclassical tearing mode control by externally driven RF current and heating, with application to ITER," *Nuclear Fusion*, vol. 59, no. 10, p. 106012, aug 2019. [Online]. Available: https://doi.org/10.1088/1741-4326/ab300f

[32] O. Sauter, M. A. Henderson, G. Ramponi, H. Zohm, and C. Zucca, "On the requirements to control neoclassical tearing modes in burning plasmas," *Plasma Physics and Controlled Fusion*, vol. 52, no. 2, p. 025002, jan 2010. [Online]. Available: https://doi.org/10.1088/0741-3335/52/2/025002

[33] W. A. Hornsby, P. Migliano, R. Buchholz, L. Kroenert, A. Weikl, A. G. Peeters, D. Zarzoso, E. Poli, and F. J. Casson, "The linear tearing instability in three dimensional, toroidal gyro-kinetic simulations," *Physics of Plasmas*, vol. 22, no. 2, p. 022118, 2015. [Online]. Available: https://doi.org/10.1063/1.4907900

[34] J. Wesson, *Tokamaks; 4th ed.*, ser. International series of monographs on physics. Oxford: Oxford Univ. Press, 2011. [Online]. Available: https://cds.cern.ch/record/1427009

[35] M. J. Choi, "Interaction between a magnetic island and turbulence," *Rev. Mod. Plasma Phys.*, vol. 5, no. 9, 2021. [Online]. Available: https://doi.org/10.1007/s41614-021-00058-w

[36] B. N. Breizman and S. E. Sharapov, "Major minority: energetic particles in fusion plasmas," *Plasma Physics and Controlled Fusion*, vol. 53, no. 5, p. 054001, mar 2011. [Online]. Available: https://doi.org/10.1088/0741-3335/53/5/054001

[37] V. Duarte, H. Berk, N. Gorelenkov, W. Heidbrink, G. Kramer, R. Nazikian, D. Pace, M. Podestà, B. Tobias, and M. V. Zeeland, "Prediction of nonlinear evolution character of energetic-particle-driven instabilities," *Nuclear Fusion*, vol. 57, no. 5, p. 054001, mar 2017. [Online]. Available: https://doi.org/10.1088/1741-4326/aa6232

[38] L. Chen, Z. Qiu, and F. Zonca, "On scattering and damping of toroidal alfvén eigenmode by drift wave turbulence," *Nuclear Fusion*, vol. 62, no. 9, p. 094001, jul 2022. [Online]. Available: https://doi.org/10.1088/1741-4326/ac7cf9

[39] A. Könies, S. Briguglio, N. Gorelenkov, T. Fehér, M. Isaev, P. Lauber, A. Mishchenko, D. A. Spong, Y. Todo, W. A. Cooper, R. Hatzky, R. Kleiber, M. Borchardt, G. Vlad, A. Biancalani, A. Bottino, and and ITPA EP TG, "Benchmark of gyrokinetic, kinetic MHD and gyrofluid codes for the linear calculation of fast particle driven TAE dynamics," *Nuclear Fusion*, vol. 58, no. 12, p. 126027, 2018. [Online]. Available: http://stacks.iop.org/0029-5515/58/i=12/a=126027

[40] A. Mishchenko, A. Könies, and R. Hatzky, "Global particle-in-cell simulations of fast-particle effects on shear Alfvén waves," *Physics of Plasmas*, vol. 16, p. 082105, 2009.

[41] A. Könies and D. Eremin, "Coupling of Alfvén and sound waves in stellarator plasmas," *Physics of Plasmas*, vol. 17, no. 1, p. 012107, 2010. [Online]. Available: https://doi.org/10.1063/1.3274921

[42] A. Könies, C. Slaby, R. Kleiber, T. Fehér, M. Borchardt, and A. Mishchenko, "The MHD continuum with a radial electric field," *Physics of Plasmas*, vol. 27, no. 12, p. 122511, 2020. [Online]. Available: https://doi.org/10.1063/5.0023961

[43] H. L. Berk, B. N. Breizman, and H. Ye, "Scenarios for the nonlinear evolution of alpha-particle-induced alfvén wave instability," *Phys. Rev. Lett.*, vol. 68, pp. 3563–3566, Jun 1992. [Online]. Available: https://link.aps.org/doi/10.1103/PhysRevLett.68.3563

[44] R. B. White, V. N. Duarte, N. N. Gorelenkov, E. D. Fredrickson, and M. Podesta, "Phase-space dynamics of alfvén mode chirping," *Physics of Plasmas*, vol. 27, no. 5, p. 052108, 2020. [Online]. Available: https://doi.org/10.1063/5.0004610

[45] X. Q. Wang, H. Wang, Y. Todo, Y. Xu, J. L. Wang, H. F. Liu, J. Huang, X. Zhang, H. Liu, J. Cheng, and C. J. Tang, "Nonlinear simulations of energetic particle-driven instabilities interacting with alfvén continuum during frequency chirping," *Plasma Physics and Controlled Fusion*, vol. 63, no. 1, p. 015004, nov 2020. [Online]. Available: https://doi.org/10.1088/1361-6587/abc3d9

[46] F. Zonca, X. Tao, and L. Chen, "A theoretical framework of chorus wave excitation," *Journal of Geophysical Research: Space Physics*, vol. 127, no. 2, p. e2021JA029760, 2022, e2021JA029760 2021JA029760. [Online]. Available: https://agupubs.onlinelibrary.wiley.com/doi/abs/10.1029/2021JA029760

[47] X. Wang, S. Briguglio, C. Di Troia, M. Falessi, G. Fogaccia, V. Fusco, G. Vlad, and F. Zonca, "Analysis of the nonlinear dynamics of a chirping-frequency alfvén mode in a tokamak equilibrium," *Physics of Plasmas*, vol. 29, no. 3, p. 032512, 2022. [Online]. Available: https://doi.org/10.1063/5.0080785

[48] C. D. Beidler, H. M. Smith, A. Alonso, T. Andreeva, J. Baldzuhn, M. N. A. Beurskens, M. Borchardt, S. A. Bozhenkov, K. J. Brunner, H. Damm, M. Drevlak, O. P. Ford, G. Fuchert, J. Geiger, P. Helander, U. Hergenhahn, M. Hirsch, U. Höfel, Y. O. Kazakov, R. Kleiber, M. Krychowiak, S. Kwak, A. Langenberg, H. P. Laqua, U. Neuner, N. A. Pablant, E. Pasch, A. Pavone, T. S. Pedersen, K. Rahbarnia, J. Schilling, E. R. Scott, T. Stange, J. Svensson, H. Thomsen, Y. Turkin, F. Warmer, R. C. Wolf,

D. Zhang, and the W7-X Team, "Demonstration of reduced neoclassical energy transport in wendelstein 7-x," *Nature*, vol. 596, no. 7871, pp. 221–226, Aug 2021. [Online]. Available: https://doi.org/10.1038/s41586-021-03687-w

[49] T. Klinger, A. Alonso, S. Bozhenkov, R. Burhenn, A. Dinklage, G. Fuchert, J. Geiger, O. Grulke, A. Langenberg, M. Hirsch, G. Kocsis, J. Knauer, A. Krämer-Flecken, H. Laqua, S. Lazerson, M. Landreman, H. Maaßberg, S. Marsen, M. Otte, N. Pablant, E. Pasch, K. Rahbarnia, T. Stange, T. Szepesi, H. Thomsen, P. Traverso, J. L. Velasco, T. Wauters, G. Weir, and T. W. and, "Performance and properties of the first plasmas of wendelstein 7-x," *Plasma Physics and Controlled Fusion*, vol. 59, no. 1, p. 014018, oct 2016. [Online]. Available: https://doi.org/10.1088/0741-3335/59/1/014018

[50] A. Dinklage, C. D. Beidler, P. Helander, G. Fuchert, H. Maaßberg, K. Rahbarnia, T. Sunn Pedersen, Y. Turkin, R. C. Wolf, A. Alonso, T. Andreeva, B. Blackwell, S. Bozhenkov, B. Buttenschön, A. Czarnecka, F. Effenberg, Y. Feng, J. Geiger, M. Hirsch, U. Höfel, M. Jakubowski, T. Klinger, J. Knauer, G. Kocsis, A. Krämer-Flecken, M. Kubkowska, A. Langenberg, H. P. Laqua, N. Marushchenko, A. Mollén, U. Neuner, H. Niemann, E. Pasch, N. Pablant, L. Rudischhauser, H. M. Smith, O. Schmitz, T. Stange, T. Szepesi, G. Weir, T. Windisch, G. A. Wurden, D. Zhang, , and the W7-X Team, "Magnetic configuration effects on the wendelstein 7-x stellarator," *Nature Physics*, vol. 14, no. 8, pp. 855–860, Aug 2018. [Online]. Available: https://doi.org/10.1038/s41567-018-0141-9

[51] R. C. Wolf, A. Alonso, S. Äkäslompolo, J. Baldzuhn, M. Beurskens, C. D. Beidler, C. Biedermann, H.-S. Bosch, S. Bozhenkov, R. Brakel, H. Braune, S. Brezinsek, K.-J. Brunner, H. Damm, A. Dinklage, P. Drewelow, F. Effenberg, Y. Feng, O. Ford, G. Fuchert, Y. Gao, J. Geiger, O. Grulke, N. Harder, D. Hartmann, P. Helander, B. Heinemann, M. Hirsch, U. Höfel, C. Hopf, K. Ida, M. Isobe, M. W. Jakubowski, Y. O. Kazakov, C. Killer, T. Klinger, J. Knauer, R. König, M. Krychowiak, A. Langenberg, H. P. Laqua, S. Lazerson, P. McNeely, S. Marsen, N. Marushchenko, R. Nocentini, K. Ogawa, G. Orozco, M. Osakabe, M. Otte, N. Pablant, E. Pasch, A. Pavone, M. Porkolab, A. Puig Sitjes, K. Rahbarnia, R. Riedl, N. Rust, E. Scott, J. Schilling, R. Schroeder, T. Stange, A. von Stechow, E. Strumberger, T. Sunn Pedersen, J. Svensson, H. Thomson, Y. Turkin, L. Vano, T. Wauters, G. Wurden, M. Yoshinuma, M. Zanini, and D. Zhang, "Performance of Wendelstein 7-X stellarator plasmas during the first divertor operation phase," *Physics of Plasmas*, vol. 26, no. 8, p. 082504, 2019. [Online]. Available: https://doi.org/10.1063/1.5098761

[52] D. Carralero, T. Estrada, E. Maragkoudakis, T. Windisch, J. Alonso, M. Beurskens, S. Bozhenkov, I. Calvo, H. Damm, O. Ford, G. Fuchert, J. García-Regaña, N. Pablant, E. Sánchez, E. Pasch, J. Velasco, and the Wendelstein 7-X team, "An experimental characterization of core turbulence regimes in wendelstein 7-x," *Nuclear Fusion*, vol. 61, no. 9, p. 096015, aug 2021. [Online]. Available: https://doi.org/10.1088/1741-4326/ac112f

[53] J. A. Alcusón, P. Xanthopoulos, G. G. Plunk, P. Helander, F. Wilms, Y. Turkin, A. von Stechow, and O. Grulke, "Suppression of electrostatic micro-instabilities in maximum-j stellarators," *Plasma Physics and Controlled Fusion*, vol. 62, no. 3, p. 035005, jan 2020. [Online]. Available: https://doi.org/10.1088/1361-6587/ab630e

[54] A. Zocco, L. Podavini, J. M. Garcìa-Regaña, M. Barnes, F. I. Parra, A. Mishchenko, and P. Helander, "Gyrokinetic electrostatic turbulence close to marginality in the wendelstein 7-x stellarator," *Phys. Rev. E*, vol. 106, p. L013202, Jul 2022. [Online]. Available: https://link.aps.org/doi/10.1103/PhysRevE.106.L013202

[55] F. Wilms, A. B. Navarro, G. Merlo, L. Leppin, T. Görler, T. Dannert, F. Hindenlang, and F. Jenko, "Global electromagnetic turbulence simulations of w7-x-like plasmas with gene-3d," *Journal of Plasma Physics*, vol. 87, no. 6, p. 905870604, 2021.

[56] C. Nührenberg, "Free-boundary ideal MHD stability of W7-X divertor equilibria," *Nuclear Fusion*, vol. 56, no. 7, p. 076010, jun 2016. [Online]. Available: https://doi.org/10.1088/0029-5515/56/7/076010

[57] S. Hirshman, W. van Rij, and P. Merkel, "Three-dimensional free boundary calculations using a spectral Green's function method," *Computer Physics Communications*, vol. 43, no. 1, pp. 143–155, 1986. [Online]. Available: https://www.sciencedirect.com/science/article/pii/0010465586900585

[58] J. Riemann, R. Kleiber, and M. Borchardt, "Effects of radial electric fields on linear ITG instabilities in W7-X and LHD," *Plasma Physics and Controlled Fusion*, vol. 58, no. 7, p. 074001, 2016. [Online]. Available: https://doi.org/10.1088/0741-3335/58/7/074001